Computers in Biology and Medicine 147 (2022) 105789

Contents lists available at ScienceDirect

Computers in Biology and Medicine

journal homepage: www.elsevier.com/locate/compbiomed

In vitro characterization and molecular dynamic simulation of shikonin as a tubulin-targeted anticancer agent

Gudapureddy Radha [a], Pradeep Kumar Naik [b], Manu Lopus [a,*]

[a] *School of Biological Sciences, UM-DAE Centre for Excellence in Basic Sciences, University of Mumbai, Vidyanagari, Mumbai, 400098, India*
[b] *Department of Biotechnology and Bioinformatics, Sambalpur University, Sambalpur, 768019, Odisha, India*

ARTICLE INFO

Keywords:
Shikonin
Tubulin
Microtubules
Triple-negative breast cancer
Molecular docking
Molecular dynamic simulation (MD simulation)

ABSTRACT

Shikonin (SK), a naphthoquinone compound from the purple gromwell, *Lithospermum erythrorhizon*, possesses a considerable antiproliferative potential. By using a combination of biophysical techniques, cellular assays, immunofluorescence imaging, and molecular dynamic simulation, we identified a possible mechanism of action of SK. SK inhibited the viability of the triple negative breast cancer cells MDA-MB-231 (IC_{50} of 1 ± 0.1 μM), and its inhibitory effect was irreversible. It strongly suppressed the clonogenic and migratory potential of the cells. Although SK did not show any phase-specific inhibition of cell cycle progression, it induced apoptosis as confirmed by annexin-V-based flow cytometry and Western immunoblotting of PARP1. Probing further into its mechanism using a tryptophan-quenching assay, it was found that SK binds the microtubule-building protein tubulin with a dissociation constant (K_d) of 8 ± 2.7 μM, without grossly damaging the tertiary structure of the protein. The drug-bound tubulin could not assemble microtubules properly *in vitro* as confirmed by polymer mass analysis, turbidimetry analysis, and transmission electron microscopy, and in cells, as visualized by immunofluorescence imaging. In cells, SK also suppressed the dynamicity of microtubules as indicated by considerable acetylation of the cellular microtubules. The fine details of tubulin-SK interactions were then elucidated using molecular docking and molecular dynamic simulation. The free energy change of the interaction ($\Delta G_{bind,pred}$) was found to be −14.60 kcal/mol and the binding involved both the intermolecular van der Waals (ΔE_{vdw}) and the electrostatic (ΔE_{ele}) interactions. Taken together, our data provide evidence for a possible mechanism of action of SK as a tubulin-targeted anticancer agent.

1. Introduction

Shikonin ((R)-5,8-Dihydroxy-2-(1-hydroxy-4-methylpent-3-en-1-yl) naphthalene-1,4-dione)) is a naphthoquinone compound present in the dried root of purple gromwell (*Lithospermum erythrorhizon)* [1]. Besides its use in cosmetics as a red colourant in lipsticks [2], and for the treatment of burns and wounds [3], SK has been known for its antibacterial and anti-inflammatory properties [4]. The anticancer potential of SK was identified three decades ago [5]. Underscoring its clinical efficacy, SK has been shown to act synergistically with many existing cancer treatment modalities, such as chemotherapy, radiotherapy, and immunotherapy [6].

Tubulin is a guanine nucleotide-containing heterodimeric protein with one alpha and one beta subunit that builds microtubules, a 24-nm-diameter, cylindrical, highly dynamic polymer [7]. Its functions in the cells range from optimization and facilitation of cell division, provision of tracks for the movement of cellular organelles and vesicles, to the maintenance of cell structure and shape. Because of its vital involvement in cellular functions and cell death, tubulin - and its filament form, microtubules - are verified targets for cancer chemotherapy. Tubulin has well-characterized binding sites for different drug molecules. For example, colchicine binds at the interface between alpha and beta tubulin [8]. Any perturbation in the finely regulated assembly dynamics of microtubules can lead to cell death [9,10].

In this study, using a combination of cellular and subcellular-level analyses, *in vitro* experiments with purified tubulin, molecular docking, and molecular dynamic simulation, we report a tubulin-targeted mechanism of action of SK in the triple-negative breast cancer cell line, MDA-MB-231.

---

* Corresponding author. School of Biological Sciences, UM-DAE Centre for Excellence in Basic Sciences, Mumbai, India.
E-mail address: manu.lopus@cbs.ac.in (M. Lopus).

https://doi.org/10.1016/j.compbiomed.2022.105789
Received 15 March 2022; Received in revised form 8 June 2022; Accepted 26 June 2022

2. Materials and methods

2.1. Materials

Shikonin (SK), taxol (Paclitaxel), colchicine, nocodazole, 8-anilino-1-naphthalenesulfonic acid (ANS), guanosine-5' -triphosphate (GTP), piperazine-N,N′-bis(2-ethanesulfonic acid) (Pipes), magnesium sulfate ($MgSO_4$), ethylene glycol tetraacetic acid (EGTA), dimethyl sulfoxide (DMSO), and bovine serum albumin (BSA) were purchased from Sigma (St. Louis, MO). Bradford reagent and glutamate were from Himedia (Mumbai, India). All other reagents were also of analytical grade.

2.2. Cell culture

MDA-MB-231 cells (American Type Culture Collection, Manassas, United States) were cultured in Dulbecco's Modified Eagle's Medium (DMEM; Himedia, India), supplemented with 10% fetal bovine serum (FBS; Himedia) and 1% penicillin and streptomycin (Himedia) [11]. The cells were maintained at 37 °C and 5% CO_2 in a humidified Forma Stericycle incubator (Thermo Fisher Scientific, Waltham, MA). The cells were free of mycoplasma as ensured by an EZkill mycoplasma elimination kit (Himedia, India).

2.3. Cell viability, clonogenicity, and cell migration assays

Trypan blue dye exclusion assay was used to determine the effect of SK on MDA-MB-231 cell viability. Briefly, MDA-MB-231 cells or the non-cancerous fibroblast cell line, L929 (5×10^4 cells/well) were seeded in 12-well, surface-treated plates for 24 h at 37 °C. They were then treated with SK (0–5 μM) for 24 h, 48 h and 72 h. After the treatment, the cells were stained with trypan blue (0.4% w/v) and counted under a light microscope [12]. DMSO was used as the vehicle control. For checking whether the effect of the drug is reversible, the cells were exposed to the drug (0–5 μM) for a short duration of 2 h. Afterwards, the drug-containing medium was replaced with drug-free medium, the cells incubated for 48 h, and the cell viability was determined, as described above. For the colony formation assay, the cells, seeded at a density of 700 cells/mL and allowed to adhere for 24 h, were treated with SK (0–1.5 μM) for an additional 24 h. After the treatment, the medium was replaced with fresh, complete medium. The cells were grown in it for eight days with one media change on the fourth day. The colonies formed were fixed with 3.7% formaldehyde for 20 min and stained with crystal violet (0.5% w/v) for 4 h. The plates were photographed and magnified digitally to count the colonies. To study the effect of SK on cell migration, the cells (1×10^5) were seeded in surface-treated 6-well plates. Upon 90% confluency, the cell layer was "wounded" by scratching it with a sterile pipette tip. The surface was then washed with 1 × PBS, photographed, and incubated in the absence or presence of SK (2 μM) for 30 h. The wounded region was photographed at specified time points (6 h, 24 h, 30 h), and the extent of wound healing was determined.

2.4. Cell cycle analysis

5×10^4 cells were seeded in 6-well surface-treated plates and allowed to grow for 24 h and were then exposed to different concentrations of SK (0–2 μM) for 48 h. Post-incubation, the cells were harvested and fixed with chilled ethanol. Following the fixation, they were treated with RNase A (200 μg/mL) for 10 min at 37 °C. The cells were then stained with propidium iodide (50 μg/mL) and analyzed in a flow cytometer (BD Accuri C6 plus, BD Biosciences, USA).

2.5. Apoptosis

The drug-treated cells were examined for possible induction of apoptosis. The annexin-V assay was performed as follows. MDA-MB-231 cells (5×10^4 cells/mL) were treated with SK (1 μM or 1.5 μM) for 48 h and stained with Alexa fluor-488 annexin-V/dead-cell apoptosis kit (Invitrogen, Eugene, OR) and analyzed in the flow cytometer mentioned above. Further, in order to ascertain apoptosis, caspase-mediated cleavage of the poly-ADP-ribose polymerase-1 (PARP1) was examined using Western Blot. Briefly, the cells treated with SK (1 μM–2 μM) for 48 h, harvested, and processed for Western immunoblot, as described previously [13]. The blots were incubated with primary antibodies for cleaved PARP1 and GAPDH (Glyceraldehyde 3-phosphate dehydrogenase; loading control; Cell Signaling Technologies, ; 1:1000 dilution, 24 h, 4 °C), followed by HRP–conjugated secondary antibodies (Cell Signaling Technologies, Danvers, MA; 1:1000 dilution, 4 h, 4 °C). The blots were then developed using SuperSignal West Pico PLUS chemiluminescent reagent (Thermo Fisher Scientific) and images were acquired using a ChemiDoc Touch imaging system (Bio-Rad, Hercules, CA).

2.6. Purification of tubulin

Tubulin was purified from fresh goat brain via cycles of polymerization and depolymerization, as described [14]. Tubulin, thus obtained, were stored at −80 °C until used.

2.7. Tryptophan-quenching assay and determination of the dissociation constant for tubulin-SK binding

Tubulin (2 μM) in PEM buffer (50 mM Pipes, 3 mM $MgSO_4$, 1 mM EGTA, pH 6.8) was incubated with different concentrations of SK (0–25 μM) for 45 min at 35 °C in a water-circulating bath. The samples were then excited at 295 nm, and the emission readings were recorded from 320 to 400 nm in a Tecan M200 Pro multimode reader (Tecan, Switzerland).

For determining the dissociation constant, first we corrected for the inner filter effect using the formula $F_{corrected} = F_{observed} \cdot \text{antilog}\,[(A_{ex} + A_{em})/2]$, where A_{ex} and A_{em} are, respectively, the absorbance at the excitation wavelength and at the emission wavelength. The dissociation constant (K_d) was determined by the formula: $1/B = K_d/[\text{free ligand}] + 1$, where B is the fractional occupancy and [free ligand] is the concentration of free SK. The fractional occupancy (B) was derived using the formula $B = \Delta F/\Delta F_{max}$. In this formula, ΔF is the change in fluorescence intensity when tubulin and SK are in equilibrium and F_{max} is the value of maximum fluorescence change when tubulin at its fully-bound state with SK. F_{max} was calculated by plotting $1/\Delta F$ versus $1/[SK]$.

2.8. Colchicine-binding assay

The colchicine-binding assay was carried out as described earlier [15]. Briefly, tubulin (3 μM) was incubated with SK (0–50 μM) in PEM buffer (35 °C, 30 min). Afterwards, the samples were incubated with colchicine (10 μM) at 35 °C for 1 h. The samples were then excited at 360 nm, and the emission spectra were recorded (390–550 nm).

2.9. Anilino-naphthalene sulfonate (ANS)-binding assay

Tubulin (2 μM) was incubated with different concentrations of SK (0–10 μM) for 30 min at 35 °C in PEM buffer. Then, ANS (50 μM) was added to the reaction mixture and incubated further at 25 °C for 20 min in the dark. The fluorescence intensity of the samples was measured after exciting them at 380 nm (emission wavelength range, 420 nm–560 nm) [16].

2.10. Microtubule polymer mass analysis and transmission electron microscopy

The ability of the tubulin to polymerize in the presence of SK was tested by polymer mass assay and turbidimetry analysis. For polymer mass assay, tubulin (12 μM) was incubated with different concentrations of SK (0–50 μM) at 35 °C in PEM buffer containing 1 mM GTP and 1 M glutamate for 45 min. After the incubation, the samples were centrifuged (27316×*g*) for 45 min at 35 °C. The supernatant was carefully aspirated off, and the pelleted polymers were incubated at 4 °C overnight in double-distilled water. The concentration of the protein in each sample was estimated by Bradford assay, using BSA as the standard. Tubulin polymerization kinetics was monitored by a turbidity assay. Briefly, tubulin (12 μM) was mixed with different concentrations of SK (0–50 μM) on ice in PEM buffer containing 1 mM GTP and 1 M glutamate. Afterwards, the absorbance of the samples was measured at 350 nm at 30 s intervals for 30 min in a Tecan M200 Pro multimode reader. For TEM, purified tubulin was incubated with SK (25 μM) or colchicine (25 μM) at 35 °C in PEM buffer for 45 min. After the assembly, the samples were fixed with 0.5% glutaraldehyde for 5 min. The TEM imaging was carried out using a field emission gun-TEM (JEM 2100 F, JEOL, Japan). The samples were analyzed at 200 kV.

2.11. Immunofluorescence imaging of cellular microtubules

MDA-MB-231 cells were grown on surface-treated coverslips for 24 h and exposed to SK (2 μM) for 24 h. They were then fixed using 4% paraformaldehyde. After washing the coverslips in 1 × PBS, the cells were incubated overnight either with mouse *anti*-ɑ-tubulin antibodies (Sigma; 1:300 dilution, 1 h, 25 °C) or with rabbit anti-acetyl-ɑ-tubulin antibodies (Cell Signaling Technologies; 1:800 dilution, 2 h, 25 °C). After this incubation with the primary antibodies, the cells were stained with Alexa-568 goat anti-mouse IgG (Invitrogen, 1:1000 dilution; 1 h; 25 °C) or Fluorescein goat anti-rabbit IgG (Invitrogen; 1:1000 dilution; 1 h; 25 °C). The cells were imaged using a spinning-disk confocal microscope (40 × , 1.3 NA (oil); Yokogawa Electric Corporation, CSU-X1, Germany).

2.12. Computational modeling and molecular dynamics simulation

2.12.1. Protein preparation

The PDB structure (PDB ID: 6Y6D [17]) of tubulin heterodimer was used in the study. Although the crystal structure of tubulin has been generated at high resolution (2.20 Å), we further refined the structure by addressing the issues of missing hydrogen atoms and missing side chain atoms of some amino acids. The amino acids were renumbered, the missing hydrogen atoms were added and the structure was preprocessed using a multistep procedure of protein preparation wizard (Schrödinger, Inc., NY). The missing side chain atoms of the amino acids were identified using Prime side-chain prediction tool and repaired using Prime (Schrödinger, Inc., NY). Furthermore, the structure was refined by energy minimization using Macromodel (Schrodinger) and OPLS 2005 force field. Polak-Ribiere Conjugate Gradient (PRCG) algorithm with an energy gradient of 0.01 kcal/mol was used for the energy minimization.

2.12.2. Preparation of molecular structure of SK

The molecular structure of SK (Fig. 1A) was built using ChemDraw and imported into Maestro (Schrödinger package). The molecular structure was energy minimized using Macromodel (Schrödinger package) and OPLS 2005 force field with PRCG algorithm (energy gradient of 0.001). We used DFT (hybrid density functional theory) with Becke's three-parameter exchange potential and the Lee-Yang-Parr correlation functional (B3LYP) with basis set 6-31G** using Jaguar (Schrödinger, package) [18] for the geometric optimization of the structure. Further, the various conformations of SK were generated using Ligprep (Schrödinger package).

2.12.3. Molecular docking of SK

We have followed a blind docking approach for the docking of SK to its suitable binding site. It is because the experimentally determined co-crystal structure of tubulin-SK complex is not yet available and, as a result, the exact binding site of SK on tubulin is unknown. In the process of the blind docking, all the binding sites of αβ-tubulin heterodimer were predicted using SiteMap (Schrodinger package) and the receptor grid boxes were generated for each predicted binding site. With the help of a Glide grid-receptor generation program, an inner grid box of size 12 Å × 12 Å x 12 Å was defined at the centroid of the binding site. Within this search space, the diameter midpoint of each docked ligand was required

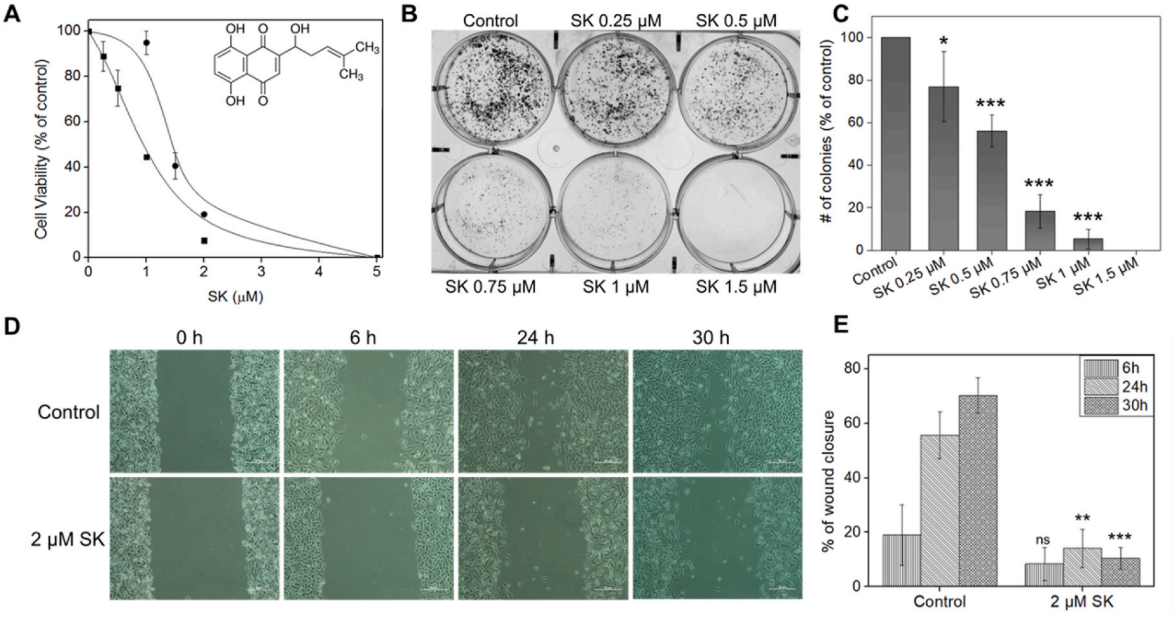

Fig. 1. Effects of SK on MDA-MB-231 cells. **A.** Inhibition of the viability of MDA-MB-231 cells after 48 h incubation with SK (0–5 μM) (solid square) ($n = 3$) and after 2 h exposure to SK (0–5 μM) (solid circles) followed by 48-h incubation with fresh medium ($n = 3$). **B.** Inhibition of colony formation of the cells by SK (0–1.5 μM). **C.** Bar graph showing the percentage of colonies formed in the presence of SK compared to the control ($n = 3$). **D.** Inhibition of cell migration in presence of SK (2 μM) manifested as a failure to 'heal' the wound made on the confluent layer of the cells. **E.** Bar graph showing the percentage of wound healing in the presence and absence of SK at different time points ($n = 3$). Data are presented as mean ± SD. The data are statistically significant at '*' ($P < 0.05$), '**' ($P < 0.01$) and '***' ($P < 0.001$), when compared to the controls.

to be present. Further, an outer grid box was also defined with an edge length of 20 Å. Herein, all ligand atoms of a valid pose must be located. The various conformations of SK thus generated were docked onto each predicted binding site using Glide XP (extra precision) algorithm (Schrodinger software package) and their binding poses evaluated using Glide XP_{Score} function [19,20]. During the docking process, Glide also conducted conformational searches for each input structure. A set of initial ligand conformations were generated through an exhaustive search of the torsional minima and the conformers are clustered in a combinatorial fashion. Each cluster characterized by a common conformation of the core and an exhaustive set of side chain conformations was docked as a single object in the first stage. The search begins with a rough positioning and scoring phase that significantly narrows the search space and reduces the number of poses to be further considered to a few hundred. These selected poses are energy minimized on precomputed OPLS-2005 van der Waals and electrostatic grids for the receptor. In the final stage, the 5–10 lowest-energy poses obtained in this fashion were subjected to a Monte Carlo sampling in which nearby torsional minima were examined and the orientation of peripheral groups of the ligand refined. The minimized poses were then rescored using the GlideScore. The algorithm generated 10000 poses, out of which only 1000 poses were used for the minimization (conjugate gradients), and the final refined structures having the lowest energy conformations were evaluated for the favorable Glide docking score. Upon completion of each docking calculation, 100 poses per ligand were generated and the best docked structure was chosen using a Glide Score (Gscore) function. The single best conformation of SK with the lowest minimum docking score was used for further analysis.

2.12.4. Molecular dynamics simulation

Molecular dynamics (MD) simulation of the best docking pose of tubulin-SK complex in the presence of GTP, GDP, and magnesium were carried out using GROMACS 2019.2 package. The docked conformation of the complex with the lowest minimum docking score was taken as the initial conformation for MD simulation. The protein was processed by Gromacs with an AMBER 999SB force field to generate coordinates and topology files. Parameters for all three ligands (GTP, GDP and SK) were estimated using a general amber force field (GAFF) implemented in Antechamber program of Amber 18. All atomic point charges were calculated using the AM1-BCC charge model. Topologies and internal coordinates for all ligands were generated using tleap program of Amber 18 and ACPYPE software [21]. The protein complex was solvated with TIP3P water model in a truncated octahedron box with a distance of 12 Å between the atoms of protein and the wall of the box. The system was neutralized by adding 0.15 mol/L Na/Cl^- ions. Counter ions at physiological ionic strength (0.15 M) were used to neutralize the system. Energy minimization was performed using the Steepest descent algorithm of 10000 steps to release conflicting contacts. After applying position restraints of 10 kcal/$Å^2$ on protein and ligands, NVT equilibration of 500 ps run was done at 300 K, followed by NPT equilibration of 500 ps with Parrinello-Rahman barostat at a reference pressure of 1 bar. After equilibration, production MD run was performed for 100 ns with a time step of 2 fs. Particle-mesh Ewald algorithm (PME) was used for long-range electrostatic interactions. Short-range electrostatics and van der Waals cut-offs were set at 10 Å. The bonds were constrained using a shake algorithm [22] and a modified Berendsen thermostat was used to regulate the temperature of the system. The atomic coordinates were recorded every 20 ps during the MD simulation. Gromacs tools were used to analyze trajectories for root mean square deviation (RMSD) and root mean square fluctuation (RMSF). All plots were generated using GRACE software. The complex structure with lowest minimum total energy from the MD trajectory was used to elucidate the binding mode of SK.

2.12.5. Predictive binding free energy of SK

In order to determine the strength of interaction between the tubulin and SK, we calculated the binding free energy ($\Delta G_{bind,pred}$) using Molecular Mechanics Poisson-Boltzmann Surface Area (MM-PBSA) [23]. From the last 10 ns of MD trajectory, a total of 500 snapshots were extracted with a time step of 20 ps, and the ensemble average of the $\Delta G_{bind,pred}$ was calculated using thermal mmgbsa. py Python script as described [21]. Additionally, the energetic contribution of the amino acids involved in the binding of SK was calculated using per-residue decomposition analysis using a Pythom scripts “MmPbSaStat.py” and MmPbSaDecomp.py”.

2.12.6. Predicted ADME properties

The QikProp program (Schrodinger package) was used to predict different ADME (absorption, distribution, metabolism, and excretion) properties of SK. Some properties having zero values were manually deleted. The program also evaluates the acceptability of the compounds based on the Lipinski’s rule of 5 (number of violations of Lipinski’s rule of five) which is essential for rational drug design. If a ligand molecule violates the rule, it likely to display impeded absorption or permeation [24].

3. Results

3.1. SK inhibited the proliferative, colony-forming, and migratory capabilities of MDA-MB-231 cells

The antiproliferative effect of SK (Fig. 1A) was examined in MDA-MB-231 breast cancer cells using a trypan blue dye-exclusion assay. SK induced a dose-dependent inhibition of cell viability. For example, 0.5 μM, 1 μM, and 2 μM SK inhibited the cell viability by 25%, 56%, and 92%, respectively, yielding a half-maximal inhibitory concentration (IC_{50}) of 1 ± 0.1 μM after 48 h incubation with the drug (Fig. 1A). The fibroblast cell line, L929, showed an IC_{50} of 2.4 ± 0.3 μM (Fig. S1C). The inhibition on cell viability was irreversible as indicated in our subsequent experiment in which the time the cells were exposed to the drug was just 2 h (Fig. 1A). The assay yielded an IC_{50} of 1.4 ± 0.03 μM. In order to check the effect of the drug on MDA-MB-231 cell viability at different time points, we performed the viability assay at 24-h and 72-h incubation with SK. As shown in Supplementary Fig. S1 A&B, SK inhibited cell viability with similar IC_{50}s at these time points. SK also inhibited, in a concentration-dependent manner, the ability of the cells to make new colonies. Specifically, 0.25 μM, 0.5 μM, and 0.75 μM of the compound reduced the number of colonies formed by 24%, 45%, and 82%, respectively, yielding an IC_{50} of 0.53 ± 0.04 μM (Fig. 1B&C). Demonstrating its ability to suppress cell migration and metastasis, SK-treated cells reduced the scratch-wound healing efficacy of the cells. Compared to the control, where the scratch made on the confluent cell layer ‘healed’ in a day’s time, the treated cells retained the wound during this period without complete healing (Fig. 1D&E). For example, 2 μM SK-treated wounds showed 8%, 14%, and 10% closure at 6 h, 24 h, and 30 h, respectively. Whereas the wound on the untreated cells showed 19%, 55%, and 70% healing at the time points mentioned above (Fig. 1D&E).

3.2. SK killed the cells via apoptosis without inducing cell cycle arrest

The effect of SK on the cell cycle progression was determined after a 48 h drug treatment. We observed a dose-dependent increase in the Sub-G_1 population of the cells without cell cycle arrest at any particular phase. Specifically, compared to the control, 1 μM, 1.5 μM, 2 μM SK increased the sub-G1 (dead cell) population by 1.6%, 13%, and 42%, respectively. (Fig. 2A&B). An annexin-V assay was employed to study the mode of SK-induced cell death in MDA-MB-231 cells. SK (1.5 μM)-treated cells showed the presence of early apoptotic, late apoptotic, and dead cells suggesting that SK promotes apoptotic cell death in this cell line (Fig. 2C&D). Further, SK treatment led to PARP1 cleavage in a concentration-dependent manner (Fig. 2E), substantiating induction of

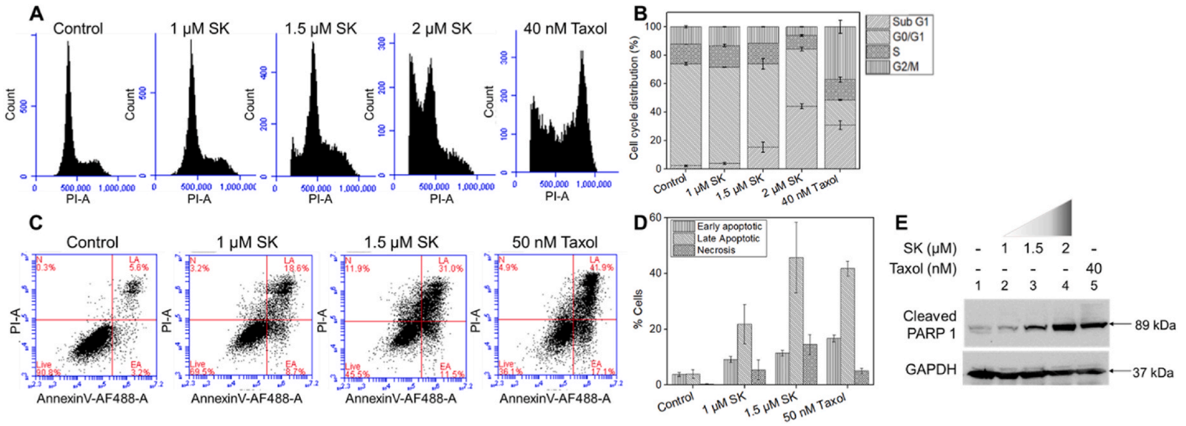

Fig. 2. A. Histograms showing a lack of phase-specific inhibition of cell cycle progression of MDA-MB-231 cells by SK (0, 1, 1.5 and 2 μM; 48 h). **B.** Bar graphs showing percentage of cells in different phases of cell cycle (n = 2). **C.** Induction of apoptosis as evidenced by annexin V-alexa fluor 488/PI staining of SK-treated (0, 1 μM and 1.5 μM; 48 h) cells. **D.** Bar diagrams showing the proportions of cells in different phases of the cell death. Cells which were positive for annexin V-Alexa fluor 488 alone (early apoptosis) or PI alone (necrosis) or both (late apoptotic) were quantified (n = 3). **E.** Western immunoblot showing cleaved PARP1 following SK treatment (0, 1, 1.5 and 2 μM; 48 h). GAPDH served as loading control (n = 2). Data are presented as mean ± SD.

apoptosis.

3.3. SK-tubulin interactions

Given that SK is a naphthoquinone compound, we next investigated their putative binding interactions with tubulin. A concentration-dependent quenching of intrinsic tryptophan fluorescence of tubulin indicated the binding of SK to the protein (Fig. 3A). Specifically, compared to the control, 2 μM, 5 μM, 10 μM, 25 μM of SK decreased the intrinsic tryptophan fluorescence by 19%, 26%, 37%, and 65%, respectively (Fig. S2A). The binding showed a dissociation constant of 8 ± 2.7 μM and 1:1 stoichiometry (Fig. 3B). A colchicine-binding assay revealed that the compound inhibits the binding of colchicine to tubulin in a concentration-dependent manner (Fig. 3C). For example, 15 μM, 25 μM and 50 μM SK decreased the tubulin-colchicine fluorescence by 29%, 42% and 60%, respectively (Fig. S2B). The presence of any possible damage to the tertiary structure of tubulin upon interaction with SK was examined with an ANS-binding assay. The compound did not enhance the tubulin-ANS fluorescence. On the contrary, it decreased ANS binding to tubulin in a concentration-dependent manner (Fig. 3D). Specifically, compared to the control, 0.5 μM, 1 μM, 2 μM, 5 μM, and 10 μM of SK decreased tubulin-ANS fluorescence by 32%, 50%, 66%, 76%, and 87%, respectively, suggesting that SK does not grossly damage the tertiary structure of the protein and that it could inhibit ANS binding to tubulin (Fig. S2C).

3.4. Inhibition of microtubule assembly by SK

The effect of SK on microtubule polymerization was assessed using a polymer mass assay, turbidimetry analysis and transmission electron microscopy. SK inhibited tubulin assembly significantly as evidenced by the polymer mass analysis. Specifically, compared to the control, 25 μM and 50 μM SK inhibited the tubulin assembly by 10% and 38%, respectively (Fig. 3E). Next, the tubulin polymerization kinetics was evaluated using turbidity measurement. Microtubule polymerization followed a typical sigmoid curve with lag, elongation and steady-state phases in untreated sample. The rate and extent of microtubule polymerization were decreased in a concentration-dependent manner by SK

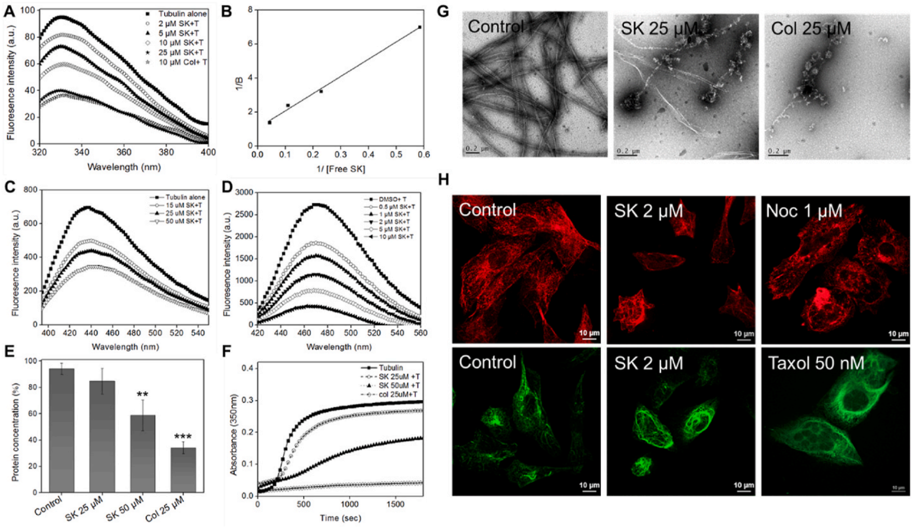

Fig. 3. Interactions of SK with purified tubulin and their manifestations on microtubule assembly *in vitro* and in cells **A.** Concentration-dependent binding of SK to purified tubulin as evidenced by the quenching of intrinsic tryptophan fluorescence of tubulin (*T*, tubulin, *col*, colchicine). B. Double-reciprocal plot showing a dissociation constant (K_d) of 8 ± 2.7 μM. C. Concentration-dependent quenching of tubulin-colchicine fluorescence in the presence of increasing concentrations of SK, indicating the binding of SK at a site near or overlapping to colchicine site **D.** Concentration-dependent decrease in tubulin-ANS fluorescence by SK, indicating inhibition of ANS binding to tubulin. **E.** Bar graph showing the inhibition of tubulin assembly by SK, as evidenced from the polymer mass analysis. (Data, ± SD; *n* = 3). The data were statistically significant at '*' ($P < 0.05$), '**' ($P < 0.01$) and '***' ($P < 0.001$), compared to the control. **F.** Turbidimetry analyses showing inhibition of the the rate and extent of tubulin assembly by SK. **G.** Electron micrographs of microtubules assembled in the absence and the presence of SK showing disruption of microtubule structural integrity. **H.** Confocal micrographs displaying SK-induced disruption of cellular microtubules (red; upper panel). *Noc,* nocodazole. Suppression of microtubule dynamicity as revealed by enhanced acetylation of the microtubules (green, lower panel).

(Fig. 3F). The effect of the compound on the microtubules was then visualized using transmission electron microscopy. The micrographs showed considerable disruption of microtubules, compared to control (Fig. 3G). Immunostaining of microtubules of MDA-MB-231 cells substantiated the *in vitro* findings. Specifically, we observed disrupted microtubule networks along with bundling of the microtubules in the treated cells (Fig. 3H, upper panel). Further, indicating a suppression of the innate dynamicity of the microtubules, considerable acetylation of microtubules in the treated cell (Fig. 3H, lower panel) was observed.

3.5. Structure validation of tubulin and molecular docking of SK onto the protein

The structure of tubulin obtained was validated using various structure validation programs such as PROCHECK, ERRAT and VERIFY3D. The ERRAT score was found to be 94.5895 and VERIFY 3D score of 98.26%. The PROCHECK results also showed 99.5% of amino acids are in the allowed region, 0.41% in the generously allowed region and only 0.1% in the disallowed region based on Ramachandran plot analysis. Taken together, all these structure validation programs revealed a good quality structure of the tubulin. Further, the structure obtained showed significant structural similarity with the crystal structure of tubulin (6Y6D) with RMSD value of 0.303 Å (Fig. S3). The binding site of SK onto tubulin is not known due to non-availability of co-crystal structure of SK-tubulin. Hence, we followed the blind docking approach to dock SK to its suitable binding site on tubulin. In this approach, we have considered all the predicted binding sites of tubulin for the docking of SK and evaluation of its docking score against all the binding sites. The binding site at the interface of α- and β-tubulin gave the lowest minimum docking score and thus was considered to be the putative binding site for SK (Table 1). This site is found to be very close to or overlapping with the colchicine binding site.

3.6. Molecular dynamic simulations and prediction of binding free energy using MM-PBSA

The docked complex of SK with tubulin was used to perform MD simulations of 100 ns to observe its stability. MM-PBSA calculation helped us to determine its predicted binding free energy ($\Delta G_{bind,pred}$). The convergence of the MD trajectories was monitored by plotting root mean square deviation (RMSD) of tubulin only, tubulin in complex with SK and SK only during 100 ns of MD simulation. The relative fluctuation in the RMSD was very small, indicating stability of the systems (Fig. S4A). Further, the relative fluctuation of the backbone Cα atoms of tubulin was also found to be very small, indicating stability of the complex (Fig. S4B). The root mean square fluctuation (RMSF) of the residues in tubulin-SK complex was found to be very small (<0.02 nm), indicating that the residues were rigid (Fig. S4C). The fluctuation in radius of gyration (Rg) of the backbone C_α atom with respect to time was also found to be minimum (<0.02 nm) over a period of 100 ns of MD simulation, indicating the stability of the system (Fig. S4D). SK was found to accommodate well inside the binding cavity (Fig. 4A and B) at the interface between α- and β-tubulin. The binding of SK involved both hydrogen bonding and hydrophobic interactions as shown in the ligplot (Fig. 4C). The binding involved four hydrogen bonds (dashed line): the oxygen atom O5 formed two hydrogen bonds, one with side-chain oxygen atom (OG1) of Thr B353 (bond length 4.35 Å) and the other with nitrogen atom (N) of Thr B353 (bond length 3.63 Å). Similarly, the oxygen atom (O2) formed a hydrogen bond with side-chain nitrogen atom (ND2) of Asn B349 and the oxygen atom (O4) formed a hydrogen bond with OH group of Tyr A210. Besides hydrogen bonding, the binding also involved hydrophobic interactions with the binding site residues (Supplementary Table S1).

Table 1
Docking results of SK with respect to different binding sites on tubulin by SiteMap. Site ID at the interface between α- and β-tubulin having the lowest minimum score, indicates the binding site for SK.

Site ID	Site score	Volume (Å)^3	Glide XP score (Kcal/mol)
1	1.0161	618.1	−7.080
2	1.0514	375.2	−6.969
3	1.0697	354.3	−4.376
4	0.84999	190.02	−4.525
5	0.8969	187.6	−4.146

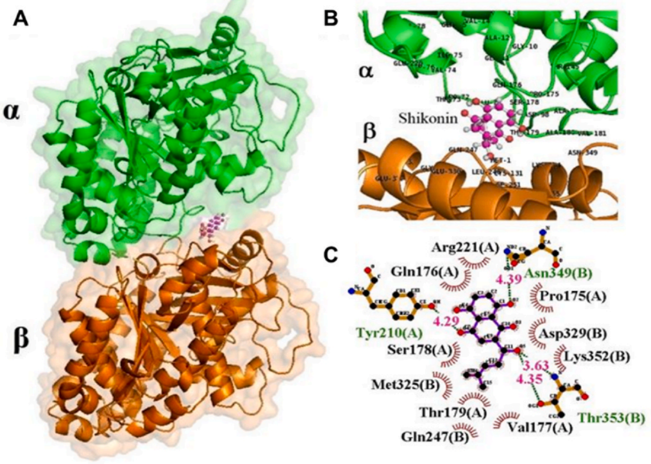

Fig. 4. Molecular docking of SK to tubulin. **A, B**. SK is accommodated well inside the binding site at the interface of α- and β-tubulin. **C.** The ligplot analysis showing the interactions of binding site amino acids with SK. Its binding involved four hydrogen bonds represented as dotted (green) lines. The amino acids involved in hydrophobic interactions are denoted with curved (red) lines.

The predictive binding free energy ($\Delta G_{bind,pred}$) of SK was determined based on MM-PBSA and was found to be −14.60 kcal/mol (Table 2). Both the intermolecular van der Waals (ΔE_{vdw}) and the electrostatic (ΔE_{ele}) interactions were significant contributors to the binding energy. Also, the non-polar solvation terms ($\Delta G_{sol\text{-}np}$), which define the burial of solvent-accessible surface-area upon binding, was favorable to the binding of SK. In contrast, the polar solvation term ($\Delta G_{SOL\text{-}PB}$) was not favorable to the binding. The charged and polar groups' desolvation penalty might have played a role here. To further understand the SK-tubulin interations at the atomic level, the predicted binding free energy contribution for each amino acid in the SK-tubulin complex was determined and plotted in Fig. 5. The amino acids having a contribution of >1.0 kcal/mol were considered as key amino acids in the binding of SK. As an example, Thr 353, Met 325, Gln 247 and Leu 248 from β-tubulin and Arg 221, Val 177 and Gln 11 from the α-tubulin have made high energy contribution (>1.0 kcal/mol) to the overall binding free energy of the complex (Fig. 5).

3.7. Predicted ADME properties of SK

A number of ADME properties were predicted viz. Molecular weight (MW), total solvent-accessible surface area (SASA), octanol/water

Table 2
Binding free energy and its components (kcal/mol) for the interaction of SK with tubulin.

Compound	ΔE_{VDW} (kcal/mol)	ΔE_{ELE} (kcal/mol)	$\Delta G_{SOL\text{-}PB}$ (kcal/mol)	$\Delta G_{SOL\text{-}NP}$ (kcal/mol)	$\Delta G_{bind\text{-}PBSA}$ (kcal/mol)
Tubulin + SK	−33.08	−9.13	31.14	−3.53	−14.60

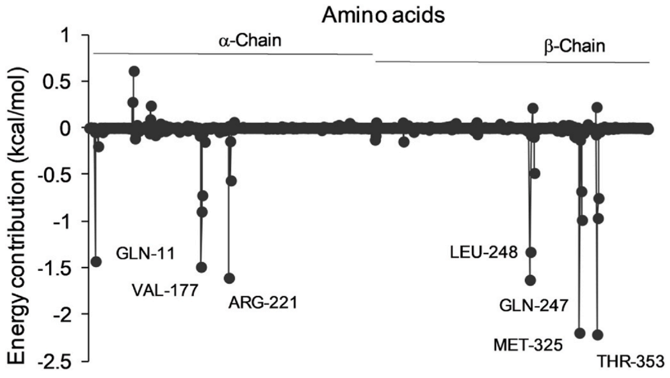

Fig. 5. The individual amino acid contribution of binding free energy to the binding of SK. The energy contribution is calculated based on MM-PBSA calculation. The amino acids having energy contribution of >1.0 kcal/mol in the binding of SK are indicated in the figure.

partition coefficient (QPlogPo/w), octanol/gas partition coefficient (QPlogPoct), water/gas partition coefficient (QPlogPw), polarizability in cubic angstroms (QPpolrz), % human oral absorption in intestine (QP %), brain/blood partition coefficient (QPlogBB), IC_{50} value for blockage of HERG K+ channel (QPlogHERG), skin permeability (QPlogKp), prediction of binding to human serum albumin (QPlogKhsa), apparent Caco-2 cell (a model for gut-blood barrier) permeability in nm/sec (QPPCaco) and apparent MDCK cell (a model for blood-brain barrier) permeability in nm/sec (QPPMDCK).

Also we evaluated the acceptability of SK based on the Lipinski's rule of 5 (number of violations of Lipinski's rule of five) which is essential for rational drug design. It was interesting to find that SK revealed significant values for the properties analyzed and qualified all the drug-like characteristics based on Lipinski's rule of 5 (Table 3).

4. Discussion

Plants serve as a repertoire for potent anticancer drugs. Several drugs used in the clinic are either obtained from plant sources or are inspired by them [25,26]. The pacific yew tree, *Taxus brevifolia*, contains the anticancer drug compound paclitaxel [27]. The Happy Tree, *Camptotheca acuminate*, possesses the template drug camptothecin, based on which, topotecan was developed [28]. The anticancer drug vinblastine was derived originally from the periwinkle plant, *Catharanthus roseaus* [29]. Podophyllotoxin from Mayapple (*Podophyllum peltatum*) inspired the development of etoposide and teniposide [30]. Plants belonging to the genus Maytenus possess the ansamycin macrolide, maytansine. The drug, Kadcyla, was developed with a derivative of maytansine [31]. In addition, a number of active substances from plants have been investigated for developing potent anticancer compounds with negligible side effects and improved treatment outcomes [32].

Table 3
A list of properties calculated for SK by Qikprop simulation and used for the ADME screening of the drug molecules.

Sl No.	ADME Screening	SK	Recommended values
1	MW	288.29	130–725
2	SASA	541.33	548.0
3	Accpt HB	4.2	2.0–20.0
4	QPpolrz	28.60	13.0–70.0
5	QPlogPoct	13.39	8.0–35
6	QPlogPw	6.10	4.0–45.0
7	QPlogPo/w	1.61	−2.0-6.5
8	QPlogHERG	2.14	Below −5.0
9	QPPCaco	142.45	<25 poor and >500 great
10	QPlogBB	−1.58	−3.0-1.2
11	QPPMDCK	60.19	<25 poor and >500 great
12	QPlogKp	−4.03	−8.0–−1.0
13	QPlogKhsa	−0.05	−1.5-1.5
14	QP%	88.05	>80% high and <25% poor
15	Rule of Five (No. of violations)	0	Maximum is 4

Given the anticancer potential of SK [33], it is important to understand the fine details of the molecular mechanism of action of this compound in the cells. Using a combination of cellular, biophysical and computational analyses, we identified a tubulin-targeted mechanism of action of SK. SK has been reported to inhibit cell viability with a low micromolar range [34,35]. Confirming these earlier reports, we found the IC_{50} of SK for MDA-MB-231 cell viability as 1 ± 0.1 μM (Fig. 1A). The fibroblast cell line, L929, showed more than twice the IC_{50} (2.4 ± 0.3 μM) for inhibiting the cell viability (Fig. S1C). We further observed that the drug's strong antiproliferative efficacy against the cells persisted even with a brief exposure (2 h) to the drug (Fig. 1A). Such irreversible drug action is known to contribute favorably to the pharmacokinetics of a drug molecule, imparting potential long-lasting clinical efficacy [36]. From a therapeutic perspective, it is noteworthy to mention here that SK does not harm normal mammary epithelial cells considerably [37]. The ability of cancer cells to migrate and colonize at different parts of the body exacerbates cancer-associated complications. SK strongly inhibited the migratory and colony-forming propensities of the highly-metastatic MDA-MB-231 cells (Fig. 1B–E). Compounds, including SK, that could inhibit these metastatic tendencies of cancers cells hold considerable clinical potential [38–40].

Using flow cytometry, we investigated whether SK inhibits cell cycle progression at any particular phase. Interestingly, the drug did not induce a phase-specific cell cycle arrest. Instead, the cells exposed to the drug directly underwent cell death as indicated by the elevated sub-G1 peak of the histogram (Fig. 2A and B), suggesting that the inhibition of cell viability does not precede cell cycle arrest. Cell cycle arrest need not be a common denominator for drug induced cell death. For example, molecules with considerable anticancer potential such as sphingosine, Br-TMB-Nos and tamoxifen-loaded solid lipid nanoparticles are known to kill cancer cells without cell cycle arrest [41–43]. The Sub-G_1 accumulation of the treated cells also suggests that the cells are killed by the drug. To confirm that the cells underwent death and also to decipher the mode of the death, we performed an annexin-V assay and Western immunoblot analyses of SK-treated cells. Annexin-V staining and cleavage of PARP1– a hallmark of apoptosis [44] confirmed apoptosis as the mode of cell death (Fig. 2C–E). Cancer cells, in general, are resistant to innate execution of apoptosis. Therefore, agents that can induce apoptosis in these cells hold a therapeutic advantage [45].

As mentioned earlier, SK is a naphthoquinone compound (hydroxy-1,4-napthquinone) [46,47]. Naphthoquinones, in general, are known to interact with tubulin and microtubules. For example, plumbagin is a naturally occurring naphthoquinone that disrupts the cellular microtubule network by binding to the colchicine site on tubulin [48]. Naphthazarin inhibits microtubule polymerization and induces apoptosis in lung cancer cells [49]. Vitamin K3 suppresses cancer cell proliferation via tubulin-binding [50] and QO-1 disrupts the structural integrity of these cytoskeletal filaments [51]. We, therefore, first tested whether the drug binds directly to purified tubulin. A tryptophan-quenching assay that detects the changes in the microenvironment of tryptophan residues of a protein upon ligand binding indicated the direct binding of the compound to tubulin (Fig. 3A&B, S2A). Using a colchicine-binding assay, we further found that SK effectively inhibits the binding of colchicine to tubulin in a concentration-dependent manner (Figs. 3C and S2B). This finding suggests that the binding site of SK on tubulin may overlap or is shared with that of colchicine at the alpha-beta tubulin interface. ANS is a fluorescent probe used for examining ligand-induced perturbations of the tertiary structure of proteins [52]. If a ligand damages the tertiary structure, enhancement of protein-ANS fluorescence can be observed [52]. SK, despite its ability to bind tubulin, did not perturb the latter's tertiary structure as evidenced by a reduction in tubulin-ANS fluorescence (Fig. 3D&S2C), indicating that despite its ability to bind tubulin, it did not grossly damage the tertiary structure of the protein. The manifestations of the binding interactions between SK and tubulin on microtubule formation was examined next. Its effect on the assembly of purified tubulin *in vitro* was probed using a polymer mass assay, turbidimetry and TEM (Fig. 3E-G). The polymer mass assay and turbidimetry analysis attested that the binding was sufficient to reduce the assembly competence of the protein (Fig. 3E&F). Moreover, the microtubules thus formed showed visible damages, as revealed by the electron micrographs (Fig. 3G). The impact of the compound on cellular microtubules was studied using immunofluorescence imaging (Fig. 3H). The disruption of microtubules was manifested in SK-treated cells as well (Fig. 3H, upper panel). In addition, considerable suppression of microtubule dynamicity (Fig. 3H, lower panel), as verified by the acetylation pattern of the cellular microtubules, was observed. Acetylation of microtubules is an indication of their suppressed dynamicity [53]. One of the characteristic features of potent microtubule-targeted therapeutics is their ability to suppress the innate dynamic instability of microtubules [54]. Even minor alterations in the dynamicity microtubules can induce cell death. Therefore, SK holds considerable potential as a microtubule-targeted anticancer agent. We next elucidated the details of SK-tubulin interactions using molecular docking followed by molecular dynamic simulations. As described in detail in the Results section, the binding of SK to tubulin involved both hydrogen bonding and hydrophobic interactions; the compound was found to fit adequately between the alpha and the beta subunits (Fig. 4D). Antitubulin agents that bind at the interface between alpha- and beta-tubulin hold strong anticancer potential. For example, DJ95 that binds at this interface has been shown to possess antiproliferative, antiangiogenic, and anti-multidrug resistance potential [55]. It has high antitumor efficacy and no significant off-target interactions. Moreover, a number of such agents are in different phases of clinical trials [56]. As well, by conjugating the drug to tumour-specific antibodies, any off-target toxicities could possibly be mitigated. Taken together, our findings suggest that SK is a tubulin-targeted agent with considerable anticancer potential.

Funding

The authors thank UM-DAE Centre for Excellence in Basic Sciences (ML) and TATA Education and Development Trust (TATA Trust- Spectrum Grant)(GR) for financial support.

Declaration of competing interest

Authors declare no conflict of interest.

Acknowledgments

We gratefully acknowledge the electron microscopy facility and the confocal microscopy facility of Indian Institute of Technology, Bombay. We also acknowledge spectrofluorometric facility at Advanced Centre for Treatment, Research and Education in Cancer (ACTREC), Navi Mumbai.

Appendix A. Supplementary data

Supplementary data to this article can be found online at https://doi.org/10.1016/j.compbiomed.2022.105789.

References

[1] X. Chen, et al., Cellular pharmacology studies of shikonin derivatives, Phytother Res. 16 (2002) 199–209, https://doi.org/10.1002/ptr.1100.

[2] K. Yazaki, Lithospermum erythrorhizon cell cultures: present and future aspects, Plant Biotechnol. 34 (2017) 131–142, https://doi.org/10.5511/plantbiotechnology.17.0823a.

[3] S.Y. Yin, et al., The phytochemical shikonin stimulates epithelial-mesenchymal transition (EMT) in skin wound healing, Evid. base Compl. Alternative Med. (2013), 262796, https://doi.org/10.1155/2013/262796.

[4] I. Andújar, et al., Pharmacological properties of shikonin - a review of literature since 2002, Planta Med. 79 (2013) 1685–1697, https://doi.org/10.1055/s-0033-1350934.

[5] N. Yoshimi, et al., Modifying effects of fungal and herb metabolites on azoxymethane-induced intestinal carcinogenesis in rats, Jpn. J. Cancer Res. 83 (1992) 1273–1278, https://doi.org/10.1111/j.1349-7006.1992.tb02758.x.

[6] J.C. Boulos, et al., Shikonin derivatives for cancer prevention and therapy, Cancer Lett. 459 (2019) 248–267, https://doi.org/10.1016/j.canlet.2019.04.033.

[7] M. Yenjerla, et al., The neuroprotective peptide NAP does not directly affect polymerization or dynamics of reconstituted neural microtubules, J. Alzheim. Dis. 19 (2010) 1377–1386, https://doi.org/10.3233/JAD-2010-1335.

[8] A.R. Chaudhuri, et al., The interaction of the B-ring of colchicine with α-Tubulin: a novel footprinting approach, J. Mol. Biol. 303 (2000) 679–692, https://doi.org/10.1006/jmbi.2000.4156.

[9] P. Hinow, et al., Modeling the effects of drug binding on the dynamic instability of microtubules, Phys. Biol. 8 (2011), 056004, https://doi.org/10.1088/1478-3975/8/5/056004.

[10] T. Mahaddalkar, M. Lopus, From natural products to designer drugs: development and molecular mechanisms action of novel anti-microtubule breast cancer therapeutics, Curr. Top. Med. Chem. 17 (2017) 2259–2568, https://doi.org/10.2174/1568026617666170104144240.

[11] J.G. Nirmala, et al., Perturbation of tubulin structure by stellate gold nanoparticles retards MDA-MB-231 breast cancer cell viability, J. Biol. Inorg. Chem. 24 (2019) 999–1007, https://doi.org/10.1007/s00775-019-01694-x.

[12] S. Dixit, et al., Synthesis, photophysical studies of positional isomers of heteroaryl BODIPYs, and biological evaluation of Di-pyrrolyl BODIPY on human pancreatic cancer cells, J. Photochem. Photobiol. Chem. 353 (2018) 368–375, https://doi.org/10.1016/j.jphotochem.2017.11.019.

[13] J.G. Nirmala, M. Lopus, Tryptone-stabilized gold nanoparticles induce unipolar clustering of supernumerary centrosomes and G1 arrest in triple-negative breast cancer cells, Sci. Rep. 9 (2019), 19126, https://doi.org/10.1038/s41598-019-55555-3.

[14] S. Pradhan, et al., Elucidation of the tubulin-targeted mechanism of action of 9-(3-pyridyl) noscapine, Curr. Top. Med. Chem. 17 (2017) 2569–2574, https://doi.org/10.2174/1568026617666170104150304.

[15] N. Nambiar, et al., Tubulin- and ROS-dependent antiproliferative mechanism of a potent analogue of noscapine, N-propargyl noscapine, Life Sci. 258 (2020), 118238, https://doi.org/10.1016/j.lfs.2020.118238.

[16] S. Cheriyamundath, et al., Insights into the structure and tubulin-targeted anticancer potential of N-(3-bromobenzyl) noscapine, Pharmacol. Rep. 71 (2019) 48–53, https://doi.org/10.1016/j.pharep.2018.09.002.

[17] M.A. Oliva, et al., Structural basis of noscapine activation for tubulin binding, J. Med. Chem. 63 (2020) 8495–8501, https://doi.org/10.1021/acs.jmedchem.0c00855.

[18] S. Santoshi, P.K. Naik, Molecular insight of isotypes specific β-tubulin interaction of tubulin heterodimer with noscapinoid, J. Comput. Aided Mol. Des. 28 (2014) 751–763, https://doi.org/10.1007/s10822-014-9756-9.

[19] R.A. Friesner, et al., Glide: a new approach for rapid, accurate docking and scoring. 1. Method and assessment of docking accuracy, J. Med. Chem. 47 (2004) 1739–1749, https://doi.org/10.1021/jm0306430.

[20] T.A. Halgren, et al., Glide: a new approach for rapid, accurate docking and scoring. 2. Enrichment factors in database screening, J. Med. Chem 47 (2004) 1750–1759, https://doi.org/10.1021/jm030644s.

[21] A.H. Arshia, et al., De novo design of novel protease inhibitor candidates in the treatment of SARS-CoV-2 using deep learning, docking, and molecular dynamic simulations, Comput. Biol. Med 139 (2021), 104967, https://doi.org/10.1016/j.compbiomed.2021.104967.

[22] J.P. Ryckaert, et al., Numerical integration of the cartesian equations of motion of a system with constraints: molecular dynamics of n-alkanes, J. Comput. Phys. 23 (1977) 327–341, https://doi.org/10.1016/0021-9991(77)90098-5.

[23] P.A. Kollman, et al., Calculating structures and free energies of complex molecules: combining molecular mechanics and continuum models, Accounts Chem. Res. 33 (2000) 889–897, https://doi.org/10.1021/ar000033j.

[24] F. Ntie-Kang, An in silico evaluation of the ADMET profile of the StreptomeDB database, SpringerPlus 2 (2013) 353, https://doi.org/10.1186/2193-1801-2-353.

[25] M.F. Mahomoodally, Traditional medicines in Africa: an appraisal of ten potent African medicinal plants, Evid. base Compl. Alternative Med. (2013), 617459, https://doi.org/10.1155/2013/617459, 2013.

[26] D.J. Newman, G.M. Cragg, K.M. Snader, Natural products as sources of new drugs over the period 1981-2002, J. Nat. Prod. 66 (2003) 1022–1037, https://doi.org/10.1021/np030096l.

[27] B.A. Weaver, How Taxol/paclitaxel kills cancer cells, Mol. Biol. Cell 25 (2014) 2677–2681, https://doi.org/10.1091/mbc.E14-04-0916.

[28] E. Martino, et al., The long story of camptothecin: from traditional medicine to drugs, Bioorg. Med. Chem. Lett 27 (2017) 701–707, https://doi.org/10.1016/j.bmcl.2016.12.085.

[29] M. Moudi, et al., Vinca alkaloids, Int. J. Prev. Med. 4 (2013) 1231–1235, https://doi.org/10.2165/00128415-200711380-00080.

[30] Z. Shah, et al., Podophyllotoxin: history, recent advances and future prospects, Biomolecules 11 (2021) 603, https://doi.org/10.3390/biom11040603.

[31] M. Lopus, Antibody-DM1 conjugates as cancer therapeutics, Cancer Lett. 307 (2011) 113–118, https://doi.org/10.1016/j.canlet.2011.03.017.

[32] W. Kooti, et al., Effective medicinal plant in cancer treatment, Part 2: review study, Journal of Evidence-Based Complementary and Alternative Medicine 22 (2017) 982–995, https://doi.org/10.1177/2156587217696927.

[33] Y.D. Jin, et al., Effect of shikonin on multidrug resistance in HepG2: the role of SIRT1, Pharmaceut. Biol. 53 (2015) 1016–1021, https://doi.org/10.3109/13880209.2014.952836.

[34] J. Xu, et al., Shikonin induces an anti-tumor effect on murine mammary cancer via p38-dependent apoptosis, Oncol. Rep. 41 (2019) 2020–2026, https://doi.org/10.3892/or.2019.6966.

[35] B. Wiench, et al., Shikonin directly targets mitochondria and causes mitochondrial dysfunction in cancer cells, Evid. base Compl. Alternative Med. (2012), https://doi.org/10.1155/2012/726025, 2012.

[36] G. Vauquelin, S.J. Charlton, Long-lasting target binding and rebinding as mechanisms to prolong in vivo drug action, Br. J. Pharmacol. 161 (2010) 488–508, https://doi.org/10.1111/j.1476-5381.2010.00936.x.

[37] Y. Chen, et al., Shikonin inhibits triple-negative breast cancer-cell metastasis by reversing the epithelial-to-mesenchymal transition via glycogen synthase kinase 3β-regulated suppression of β-catenin signaling, Biochem. Pharmacol. 166 (2019) 33–45, https://doi.org/10.1016/j.bcp.2019.05.001.

[38] F. Wang, et al., Shikonin inhibits cancer through P21 upregulation and apoptosis induction, Front. Pharmacol. 11 (2020) 1088, https://doi.org/10.3389/fphar.2020.00861.

[39] L. Sha, et al., Shikonin inhibits the Warburg effect, cell proliferation, invasion and migration by downregulating PFKFB2 expression in lung cancer, Mol. Med. Rep. 24 (2021) 560, https://doi.org/10.3892/mmr.2021.12199.

[40] C. Bao, et al., Shikonin inhibits migration and invasion of triple-negative breast cancer cells by suppressing epithelial-mesenchymal transition via miR-17-5p/PTEN/Akt pathway, J. Cancer 12 (2021) 76–88, https://doi.org/10.7150/JCA.47553.

[41] E.H. Ahn, et al., Sphingosine induces apoptosis and down-regulation of MYCN in PAX3-FOXO1-positive alveolar rhabdomyosarcoma cells irrespective of TP53 mutation, Anticancer Res. 38 (1) (2018) 71–76, https://doi.org/10.21873/anticanres.12193.

[42] T. Mahaddalkar, et al., Subtle alterations in microtubule assembly dynamics by Br-TMB-Noscapine strongly suppress triple-negative breast cancer cell viability without mitotic arrest, ChemistrySelect 1 (2016) 4313–4319, https://doi.org/10.1002/slct.201600959.

[43] R. Abbasalipourkabir, et al., Tamoxifen-loaded solid lipid nanoparticles-induced apoptosis in breast cancer cell lines, J. Exp. Nanosci. 11 (3) (2016) 161–174, https://doi.org/10.1080/17458080.2015.1038660.

[44] G.V. Chaitanya, et al., PARP-1 cleavage fragments: signatures of cell-death proteases in neurodegeneration, Cell Commun. Signal. 8 (2010) 31, https://doi.org/10.1186/1478-811X-8-31.

[45] B. Ke, et al., Targeting programmed cell death using small-molecule compounds to improve potential cancer therapy, Med. Res. Rev. 36 (2016) 983–1035, https://doi.org/10.1002/med.21398.

[46] C.E. Pereyra, et al., The diverse mechanisms and anticancer potential of naphthoquinones, Cancer Cell Int. 19 (2019) 207, https://doi.org/10.1186/s12935-019-0925-8.

[47] T. Kayashima, et al., 1,4-Naphthoquinone is a potent inhibitor of human cancer cell growth and angiogenesis, Cancer Lett. 278 (2009) 34–40, https://doi.org/10.1016/j.canlet.2008.12.020.

[48] B.R. Acharya, B. Bhattacharyya, G. Chakrabarti, The natural naphthoquinone plumbagin exhibits antiproliferative activity and disrupts the microtubule network through tubulin binding, Biochemistry 47 (2008) 7838–7845, https://doi.org/10.1021/bi800730q.

[49] B.R. Acharya, et al., The microtubule depolymerizing agent naphthazarin induces both apoptosis and autophagy in A549 lung cancer cells, Apoptosis 16 (2011) 924–939, https://doi.org/10.1007/s10495-011-0613-1.

[50] B.R. Acharya, et al., Vitamin K3 disrupts the microtubule networks by binding to tubulin: a novel mechanism of its antiproliferative activity, Biochemistry 48 (2009) 6963–6974, https://doi.org/10.1021/bi900152k.

[51] H. Sato, et al., New 2-aryl-1,4-naphthoquinone-1-oxime methyl ether compound induces microtubule depolymerization and subsequent apoptosis, J. Pharmacol. Sci. 118 (2012) 467–478, https://doi.org/10.1254/jphs.11229FP.

[52] B. Bhattacharyya, J. Wolff, The interaction of 1-anilino-8-naphthalene sulfonate with tubulin: a site independent of the colchicine-binding site, Arch. Biochem. Biophys. 167 (1975) 264–269, https://doi.org/10.1016/0003-9861(75)90462-2.

[53] Y. Nekooki-Machida, H. Hagiwara, Role of tubulin acetylation in cellular functions and diseases, Med. Mol. Morphol. 53 (2020) 191–197, https://doi.org/10.1007/s00795-020-00260-8.

[54] L. Wilson, et al., Effects of eribulin on microtubule binding and dynamic instability are strengthened in the absence of the βIII tubulin isotype, Biochemistry 54 (42) (2015) 6482–6489, https://doi.org/10.1021/acs.biochem.5b00745.

[55] K.E. Arnst, et al., Colchicine binding site agent DJ95 overcomes drug resistance and exhibits antitumor efficacy, Mol. Pharmacol. 96 (2019) 73–89, https://doi.org/10.1124/mol.118.114801.

[56] E.C. McLoughlin, N.M. O'boyle, Colchicine-binding site inhibitors from chemistry to clinic: a review, Pharmaceuticals 13 (2020) 8, https://doi.org/10.3390/ph13010008.